PROCEEDINGS A

royalsocietypublishing.org/journal/rspa

Research

Cite this article: Lu L, Dang X, Feng F, Lv P, Duan H. 2022 Conical Kresling origami and its applications to curvature and energy programming. *Proc. R. Soc. A* **477**: 20210712. https://doi.org/10.1098/rspa.2021.0712

Received: 8 September 2021
Accepted: 29 November 2021

Subject Areas:
mechanics, applied mathematics, mechanical engineering

Keywords:
conical Kresling origami, bistability, curvature programming, energy programming, inverse design

Author for correspondence:
Huiling Duan
e-mail: hlduan@pku.edu.cn

Electronic supplementary material is available online at https://doi.org/10.6084/m9.figshare.c.5758641.

THE ROYAL SOCIETY PUBLISHING

Conical Kresling origami and its applications to curvature and energy programming

Lu Lu[1], Xiangxin Dang[1], Fan Feng[2], Pengyu Lv[1] and Huiling Duan[1,3]

[1]State Key Laboratory for Turbulence and Complex Systems, Department of Mechanics and Engineering Science, BIC-ESAT, College of Engineering, Peking University, Beijing 100871, People's Republic of China
[2]Cavendish Laboratory, University of Cambridge, Cambridge CB3 0HE, UK
[3]CAPT, HEDPS and IFSA, Collaborative Innovation Center of MoE, Peking University, Beijing 100871, People's Republic of China

LL, 0000-0001-6167-9158; XD, 0000-0003-0737-9597; FF, 0000-0002-5456-670X; HD, 0000-0003-1478-5649

Kresling origami has recently been widely used to design mechanical metamaterials, soft robots and smart devices, benefiting from its bistability and compression-twist coupling deformation. However, previous studies mostly focus on the traditional parallelogram Kresling patterns which can only be folded to cylindrical configurations. In this paper, we generalize the Kresling patterns by introducing free-form quadrilateral unit cells, leading to diverse conical folded configurations. The conical Kresling origami is modelled with a truss system, by which the stable states and energy landscapes are derived analytically. We find that the generalization preserves the bistable nature of parallelogram Kresling patterns, while enabling an enlarged design space of geometric parameters for structural and mechanical applications. To demonstrate this, we develop inverse design frameworks to employ conical Kresling origami to approximate arbitrary target surfaces of revolution and achieve prescribed energy landscapes. Various numerical examples obtained from our framework are presented, which agree well with the paper models and the finite-element simulations. We envision that the proposed conical Kresling pattern and inverse design framework can provide a new

perspective for applications in deployable structures, shape-morphing devices, multi-modal robots and multistable metamaterials.

1. Introduction

Origami is the craft of folding paper that can transform simple two-dimensional (2D) flat sheets into complex three-dimensional (3D) structures. Such folding procedures can introduce many unique mechanical properties coupled with geometric constraints, such as negative Poisson's ratio [1,2], rigid-foldability [3,4] and multistability [5,6]. In recent years, origami principles have become an ideal platform for designing deployable and functional structures. A wide range of such applications have been carried out, including deployable space solar panels [7], medical stents [8], mechanical metamaterials [9–14], architectural building blocks [15–17], inflatable shelters [18], soft robots [19–21] and shape-programmable origami tessellations [22–28].

In the rich and colourful origami gallery, a large class of classical origami is composed of tessellated periodic unit cells, such as the Miura [29], helical Miura [5], Kresling [30], square-twist [31] and waterbomb [32] patterns. Among these periodic origami patterns, Kresling pattern—originally discovered by the architect Biruta Kresling when conducting the twist buckling experiments of thin-walled cylinders [30]—partakes of its bistability and compression-twist coupling deformation characteristics. When subjected to an axial force or torque that is sufficiently large, the Kresling origami structure will jump from one stable state to the other through a coupled deformation of axial translation and rotation [33–35]. Harnessing the bistability and the compression-twist coupling motion, Kresling origami has enabled the design of stiffness-tunable mechanical metamaterials [36–38], impact mitigation systems [39], crawling or grasping robots [40–42] and smart control devices [43–45].

The periodicity of origami patterns (including the Kresling origami) significantly simplifies the analysis of global properties such as foldability and multistability, as well as the fabrication process. However, the shapes and mechanical responses of these origami become periodic and restrictive in some sense. For the inverse design of origami in attempts to achieve target folded shapes or energy landscapes, one has to generate free-form crease patterns to break the periodicity. For example, Tachi [4] generalized the well-known Miura-ori and derived the geometric conditions for realizing rigidly and flat-foldability of general quadrilateral mesh origami. Based on this generalization, various optimization algorithms have been developed to determine the quadrilateral mesh patterns that can approximate curved surfaces [3,23–26]. Besides, the inverse design of 3D origami tessellation has been achieved by using the generalized Resch's pattern [27] and the generalized waterbomb pattern [28]. However, such a generalization and the related applications in inverse design have not been realized for traditional Kresling origami (TKO), limited by its parallelogram unit cells and cylindrical folded configuration. To broaden the design space and fully unlock the application potentiality of Kresling origami, in this paper, we generalize the traditional parallelogram Kresling origami by introducing general quadrilateral unit cells with additional degrees of freedom, and obtain a new Kresling pattern with a conical folded configuration instead of the traditional cylindrical one. We expect that the conical Kresling origami (CKO) can serve as a promising candidate for the design of multistable structures with desired folded configurations and energy landscapes.

To this end, we firstly present a generalized design framework for CKO composed of general quadrilateral unit cells, and derive the analytical solutions and design spaces of its stable states. The phase diagrams characterizing the stability are illustrated for multiple examples with different geometric parameters. Then, we solve two inverse problems to demonstrate the functional applications of the CKO in two different aspects: curvature programming and energy programming. For the first demonstration, we use CKO tessellations to approximate arbitrary curved surfaces of revolution. For the second one, we design multistable CKO tessellations with prescribed stable-state heights and energy barriers. We also fabricate paper models and perform

finite-element (FE) simulations to support the validity of the numerical results of our inverse design. These two demonstrations show that the CKO has potential capabilities in applications that need target shapes (e.g. origami antenna [46]) or target mechanical responses (e.g. origami structures for energy absorption [47,48]).

2. Conical Kresling origami

We start by introducing the geometry of the TKO and the CKO. As shown in figure 1*a*, the reference crease pattern of a TKO comprises an array of congruent parallelogram unit cells. By folding along the mountain and valley creases and connecting the two ends of the flat sheet in a compatible manner, the TKO can form a cylindrical structure with helical symmetry. Instead, by using an array of congruent general convex quadrilateral unit cells and following the same folding process of the TKO, a conical structure can be obtained (figure 1*b*). Here, we define this new pattern as the CKO. The representative unit cells of the CKO can be characterized by four geometric parameters: the top edge length a, the bottom edge length b, the side edge length c (i.e. the mountain crease) and the angle β between the bottom edge and the mountain crease. Note that the neighbouring unit cells share the same mountain crease, therefore, the opposite side lengths of the quadrilateral unit cell are equal. Then, the length of the valley crease can be expressed as

$$d = \sqrt{b^2 + c^2 - 2bc\cos\beta}. \tag{2.1}$$

(a) Theoretical modelling

Next, we develop a theoretical model to investigate the stability of the CKO. Since the Kresling origami is not rigidly foldable [44,45], its triangular facet may experience bending or warping upon folding. It is therefore difficult to accurately describe its mechanical behaviours with a theoretical model. To overcome this issue, following many previous works [36,38,45], we assume that the elastic energy change of the CKO during the folding process is mainly induced by the crease stretching or shortening, and the bending energy of the facets and the folding energy of the creases are negligible [49]. Under this assumption, the CKO is equivalent to a truss model shown in figure 2*a*. Such a truss model has been proved to be accurate and effective in capturing the elastic behaviours of TKO structures [38,45,49]. In this way, the elastic energy of the CKO can be represented by the total strain energy of its creases (i.e. trusses), which can be written as [36,45]

$$U = \frac{nk_m}{2}(\tilde{c} - c)^2 + \frac{nk_v}{2}(\tilde{d} - d)^2, \tag{2.2}$$

where n is the number of unit cells, $k_m = EA/c$ and $k_v = EA/d$ are the stiffness coefficients of the mountain creases and the valley creases, respectively, E is the elastic modulus, and A is the cross-section area. $\tilde{c}$ and $\tilde{d}$ are the lengths of the mountain creases and the valley creases during folding, respectively.

Figure 2*b* is the top view of the CKO truss model, in which B_i' $(i = 1, 2, \ldots, n)$ is the projection of B_i onto the bottom surface. The radii of the circumcircles of the top and bottom surfaces, r and R, can be calculated by

$$r = \frac{a}{2\sin(\pi/n)} \quad \text{and} \quad R = \frac{b}{2\sin(\pi/n)}. \tag{2.3}$$

From this diagram, we can obtain that

$$\tilde{c}(h, \varphi) = \sqrt{h^2 + \overline{A_1B_1'}^2} = \sqrt{h^2 + r^2 + R^2 - 2rR\cos\varphi} \tag{2.4}$$

and

$$\tilde{d}(h, \varphi) = \sqrt{h^2 + \overline{A_1B_2'}^2} = \sqrt{h^2 + r^2 + R^2 - 2rR\cos\left(\varphi + \frac{2\pi}{n}\right)}, \tag{2.5}$$

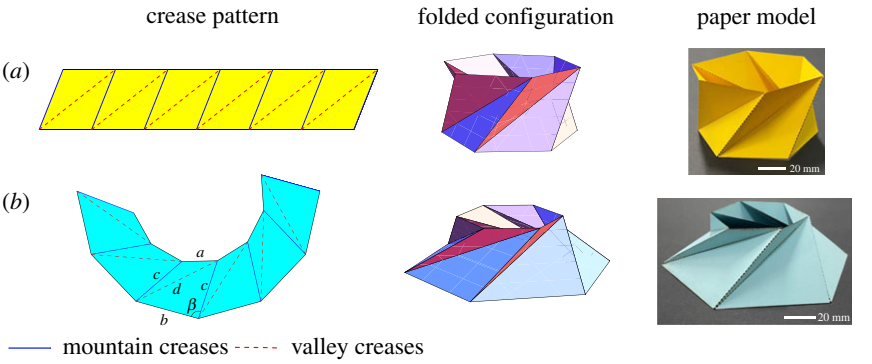

Figure 1. Schematics of (*a*) a TKO composed of parallelogram unit cells, and its cylindrical folded configuration, (*b*) a CKO composed of general convex quadrilateral unit cells, and its conical folded configuration. (Online version in colour.)

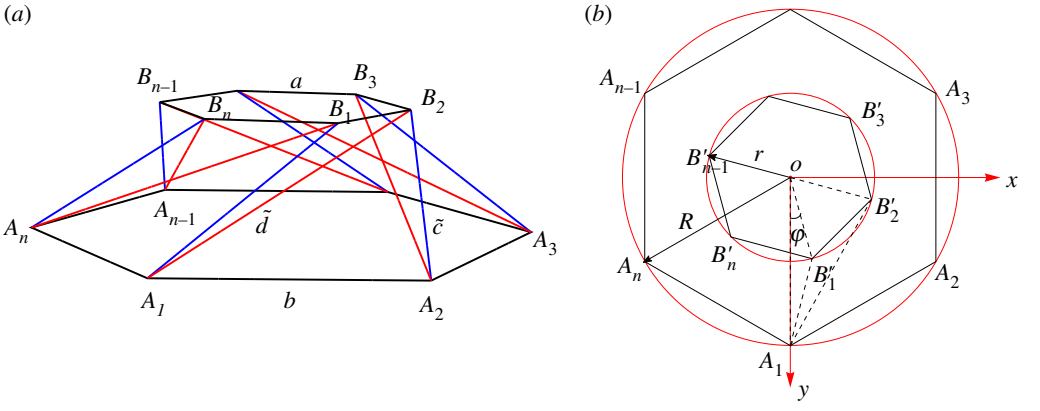

Figure 2. Truss model for CKO. (*a*) 3D view. The red and blue lines represent the valley creases and the mountain creases, respectively. The black lines denote the bottom and top frames. (*b*) Top view. B'_i ($i = 1, 2, \ldots, n$) is the projection of B_i onto the bottom surface. The two red circles are the circumcircles of the bottom and top surfaces. (Online version in colour.)

where h is the height of the CKO and φ is the relative twist angle of the top and bottom surfaces. The pair (h, φ) can be used to represent an intermediate state upon folding. Here, φ should satisfy

$$0 \le \varphi \le \min\{\varphi_f, \varphi_s\}, \tag{2.6}$$

where φ_f corresponds to the folded-flat state (i.e. $h = 0$), and $\varphi_s = \pi - 2\pi/n$ associates with the locked state, which means that exceeding this twist angle, the crease lines will intersect each other.

(b) Analytical solutions for stable states

Subsequently, we derive the analytical solutions for the stable states of CKO based on the truss model. According to equations (2.2)–(2.5), the elastic energy U depends on two variables, h and φ. To find the stable states of the CKO, we take derivatives of the elastic energy with respect to h and φ, respectively, and obtain

$$\frac{\partial U}{\partial h} = nk_m(\tilde{c} - c)\frac{\partial \tilde{c}}{\partial h} + nk_v(\tilde{d} - d)\frac{\partial \tilde{d}}{\partial h} \tag{2.7}$$

and

$$\frac{\partial U}{\partial \varphi} = nk_m(\tilde{c} - c)\frac{\partial \tilde{c}}{\partial \varphi} + nk_v(\tilde{d} - d)\frac{\partial \tilde{d}}{\partial \varphi}. \tag{2.8}$$

By setting the two derivatives to zero, and then substituting equations (2.4) and (2.5), we have

$$k_m h\left(1 - \frac{c}{\tilde{c}}\right) + k_v h\left(1 - \frac{d}{\tilde{d}}\right) = 0 \tag{2.9}$$

and

$$k_m\left(1 - \frac{c}{\tilde{c}}\right)\sin\varphi + k_v\left(1 - \frac{d}{\tilde{d}}\right)\sin\left(\varphi + \frac{2\pi}{n}\right) = 0. \tag{2.10}$$

Obviously, $h = 0$ is a solution of equation (2.9). Substituting it into equation (2.10), the relative twist angle φ_f at the folded-flat state can be determined. Thus, we get a stationary point (h_f, φ_f) with $h_f = 0$. In the electronic supplementary material, we show that under certain conditions, (h_f, φ_f) is a local minimum point of the elastic energy $U(h, \varphi)$, corresponding to a folded-flat non-zero-energy stable state of the CKO.

Moreover, when $h \neq 0$, substituting equation (2.9) into equation (2.10), and applying the identity $\sin(\varphi + 2\pi/n) - \sin\varphi = 2\cos(\varphi + \pi/n)\sin(\pi/n)$, one can obtain that

$$2k_v\left(1 - \frac{d}{\tilde{d}}\right)\cos\left(\varphi + \frac{\pi}{n}\right)\sin\frac{\pi}{n} = 0, \tag{2.11}$$

which gives the necessary conditions for a stable state

$$\varphi = \frac{\pi}{2} - \frac{\pi}{n} \quad \text{or} \quad \tilde{d} = d. \tag{2.12}$$

By inserting $\varphi = \pi/2 - \pi/n$ into equation (2.9), the corresponding height h_0 can be determined. Then we obtain a stationary point (h_0, φ_0), in which $\varphi_0 = \pi/2 - \pi/n$. It can be proved that for a bistable CKO with two zero-energy stable states, (h_0, φ_0) is a saddle point of the energy surface $U(h, \varphi)$ (see Proof 1 in electronic supplementary material), while it is a maximum point of the curve on the energy surface $U(h, \varphi)$ determined by $\partial U/\partial h = 0$ or $\partial U/\partial \varphi = 0$ (see Proofs 2 and 3 in electronic supplementary material).

For $\tilde{d} = d$ and $h \neq 0$, equation (2.9) implies $\tilde{c} = c$. Then the lengths of creases in the reference states and the folded states are the same. In this case, $U(h, \varphi) = 0$ and the CKO is at a zero-energy and trivially stable state. Therefore, the condition for the CKO with zero-energy stable state is that the creases preserve their original lengths, which can be expressed as

$$\left.\begin{aligned} &\sqrt{h^2 + r^2 + R^2 - 2rR\cos\varphi} = c \\ \text{and} \quad &\sqrt{h^2 + r^2 + R^2 - 2rR\cos\left(\varphi + \frac{2\pi}{n}\right)} = d. \end{aligned}\right\} \tag{2.13}$$

Substituting the first equation of equation (2.13) into the second one yields

$$\cos\varphi - \cos\left(\varphi + \frac{2\pi}{n}\right) = \frac{d^2 - c^2}{2rR}. \tag{2.14}$$

By introducing equations (2.1) and (2.3), and using the trigonometric identity $\cos\varphi - \cos(\varphi + 2\pi/n) = 2\sin(\varphi + \pi/n)\sin(\pi/n)$, equation (2.14) can be rewritten as

$$\sin\left(\varphi + \frac{\pi}{n}\right) = \frac{b - 2c\cos\beta}{a}\sin\frac{\pi}{n}. \tag{2.15}$$

Under the condition in equation (2.6), equation (2.15) has at most two solutions, which suggests that the CKO has at most two zero-energy stable states. The number of the stable states depends on the geometric parameters of its unit cells. To identify this, we discuss this problem in three cases, according to the order of occurrence of the two critical states (i.e. folded-flat state and locked state) upon folding. For simplicity, we define $\lambda = ((b - 2c\cos\beta)/a)\sin(\pi/n)$.

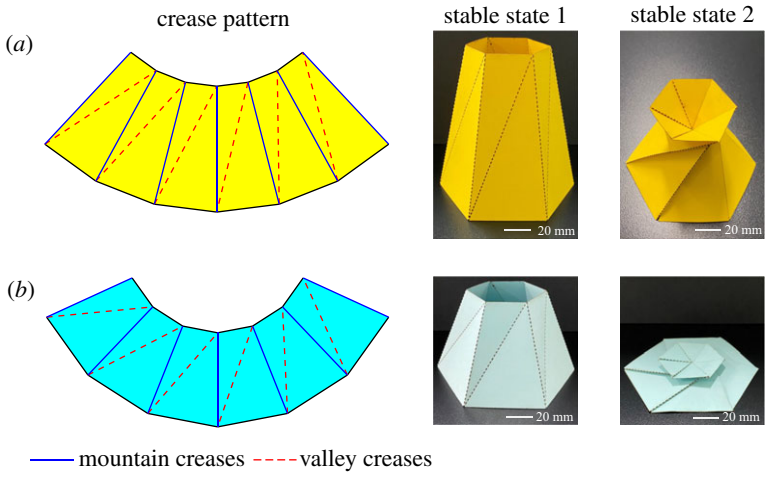

Figure 3. Crease patterns and stable-state configurations of bistable CKO composed of isosceles trapezoid unit cells. (*a*) A non-flat-foldable CKO with geometric parameters $a = 1, b = 2$ and $c = 4$. (*b*) A flat-foldable CKO with geometric parameters $a = 1$, $b = 2$ and $c = \sqrt{7}$. The number of unit cell is 6. (Online version in colour.)

Case 1: Folded-flat state and locked state occur simultaneously. In this case, we have $\varphi_f = \varphi_s = \pi - 2\pi/n$, which gives $c = c_{fs} \triangleq \sqrt{r^2 + R^2 + 2rR\cos(2\pi/n)}$ based on equation (2.10). The point $(h_f, \varphi_f) = (0, \pi - 2\pi/n)$ corresponds to the folded-flat zero-energy stable state of a CKO composed of isosceles trapezoid unit cells (figure 3*b*). We will discuss this special crease pattern in detail in remark 2.1.

Case 2: Locked state occurs first. When the locked state takes place first upon folding, we have $\varphi_s < \varphi_f$, which leads to $c > c_{fs}$. In this case, the CKO cannot be folded flat (i.e. h cannot be zero), and the relative twist angle φ needs to satisfy $0 \le \varphi \le \varphi_s$ based on equation (2.6). Consequently, when $\sin(\pi/n) \le \lambda < 1$, equation (2.15) has two solutions for φ within this range, and accordingly the CKO has two zero-energy stable states, which are given by

$$(h_1, \varphi_1) = \left(\sqrt{c^2 - r^2 - R^2 + 2rR\cos\varphi_1}, \arcsin\lambda - \frac{\pi}{n}\right) \tag{2.16}$$

and

$$(h_2, \varphi_2) = \left(\sqrt{c^2 - r^2 - R^2 + 2rR\cos\varphi_2}, \pi - \arcsin\lambda - \frac{\pi}{n}\right). \tag{2.17}$$

Particularly, when $\lambda = 1$, we have $\varphi_1 = \varphi_2 = \varphi^*$ and $h_1 = h_2 = h^*$, and equation (2.15) has only one solution for φ, which implies that the CKO has only one zero-energy stable state at

$$(h^*, \varphi^*) = \left(\sqrt{c^2 - r^2 - R^2 + 2rR\sin\frac{\pi}{n}}, \frac{\pi}{2} - \frac{\pi}{n}\right). \tag{2.18}$$

Coincidentally, when $\lambda = 1$, one can prove that the point (h_0, φ_0) also reaches the stable-state point (h^*, φ^*) (see Proof 4 in electronic supplementary material). Then all the stationary points correspond to the same zero-energy state, i.e. the stable state.

Case 3: Folded-flat state occurs first. When the folded-flat state occurs first upon folding, we have $\varphi_f < \varphi_s$, which results in $c < c_{fs}$. Under this condition, we can obtain from equation (2.6) that $0 \le \varphi \le \varphi_f$. Moreover, we know from equations (2.16) and (2.17) that $\varphi_1 + \varphi_2 = \varphi_s = 2\varphi_0 = \pi - 2\pi/n$. Without loss of generality, assuming $\varphi_1 \le \varphi_2$, we have $\varphi_1 \le \varphi_0 \le \varphi_2 < \varphi_s$. In the following, we discuss the number of stable states of the CKO based on φ_f compared with φ_0, φ_1 and φ_2.

(i) When $\varphi_2 \le \varphi_f < \varphi_s$, we have $\sin(\pi/n + \varphi_f) \le \lambda \le 1$. In this case, if $\lambda \ne 1$, equation (2.15) has two solutions φ_1 and φ_2, and accordingly the CKO has two zero-energy stable states given

by equations (2.16) and (2.17). Otherwise if $\lambda = 1$, equation (2.15) has only one solution φ^*, indicating that the CKO has only one zero-energy stable state given by equation (2.18).

(ii) When $\varphi_0 < \varphi_f < \varphi_2$, we have $\sin(\pi/n) \le \lambda < \sin(\pi/n + \varphi_f)$. In this case, equation (2.15) has only one solution φ_1, which suggests that the CKO has only one zero-energy stable state, i.e. equation (2.16). However, the stationary point (h_f, φ_f) corresponding to the folded-flat state is a local minimum point of the elastic energy $U(h, \varphi)$ in this situation (see Proof 5 in electronic supplementary material), which provides a non-zero-energy stable state for the CKO. Therefore, the CKO is also bistable.

(iii) When $\varphi_1 \le \varphi_f \le \varphi_0$, we have $\sin(\pi/n) \le \lambda \le \sin(\pi/n + \varphi_f)$. In this case, equation (2.15) has only one solution φ_1 and (h_f, φ_f) is not a local minimum point, indicating that the CKO has only one zero-energy stable state given by equation (2.16).

Remark 2.1. When the quadrilateral unit cell is an isosceles trapezoid, one can find that $a = b - 2c\cos\beta$. Under this condition, equation (2.15) reduces to $\sin(\varphi + \pi/n) = \sin(\pi/n)$, and the two solutions of the relative twist angle are $\varphi_1 = 0$ and $\varphi_2 = \pi - 2\pi/n$. Substituting φ_1 and φ_2 into equations (2.16) and (2.17), the two stable states can be obtained as

$$(h_1, \varphi_1) = (\sqrt{c^2 - r^2 - R^2 + 2rR}, 0) \tag{2.19}$$

and

$$(h_2, \varphi_2) = \left(\sqrt{c^2 - r^2 - R^2 - 2rR\cos\frac{2\pi}{n}}, \pi - \frac{2\pi}{n}\right). \tag{2.20}$$

From equations (2.19) and (2.20), we find that when $R - r < c < c_{fs}$, the second solution equation (2.20) does not exist, and the CKO composed of isosceles trapezoid unit cells has only one stable state, i.e. equation (2.19). But when $c \ge c_{fs}$, both solutions exist, and the CKO has two stable states. For the latter case, the length of the mountain crease c is in the range that makes the locked state occur first ($c > c_{fs}$) or makes the two critical states take place simultaneously ($c = c_{fs}$). In figure 3, we give two typical examples for this special circumstance, including a non-flat-foldable bistable CKO with $c > c_{fs}$, and a flat-foldable bistable CKO with $c = c_{fs}$. It is interesting that the second stable state of the bistable CKO consisting of isosceles trapezoid unit cells always occurs at the locked state upon folding, making the structure to be self-locked. Moreover, since our theoretical model does not consider the folding stiffness of the creases and the thickness of the paper, the folded-flat state of our physical model is not strictly flat.

To better understand the relationship between the geometric parameters and the number of stable states, we plot the phase diagram of stable states for CKO structures with $a = 1$ and $b = 2$ in figure 4 based on the above analytical solutions. As can be seen, in the yellow area as well as at the *AB*, *AF*, *BF* and *EF* boundaries, the CKO is monostable. In the red area as well as at the *BC* boundary, the CKO is bistable, and has a zero-energy stable state and a folded-flat non-zero-energy stable state. In the green area as well as at the *CD* and *CF* boundaries, the CKO is also bistable, but has two zero-energy stable states. Outside these areas, the geometric parameters do not correspond to a quadrilateral unit cell, or the quadrilateral unit cell cannot form a stable CKO. The analytical expressions of the boundaries are summarized below:

— At the *ABCD* boundary: $b - 2c\cos\beta = a$, and the CKO consists of isosceles trapezoid unit cells and its stable states are given by equations (2.19) and (2.20).
— At the *EF* boundary: $\lambda = 1$, and the stable state of the CKO is given by equation (2.18).
— At the *AFC* boundary: $\lambda = \sin(\pi/n + \theta)$ with $\theta = \arccos((r^2 + R^2 - c^2)/2rR)$, and the CKO has a folded-flat zero-energy stable state at $(h_2, \varphi_2) = (0, \theta)$.
— At the *BF* boundary, the relative twist angle φ_f of the CKO at the folded-flat state equals φ_0.

Several representative configurations for the monostable and bistable CKO structures are also presented in figure 4. We can observe that for the same geometric parameters, with the increase of

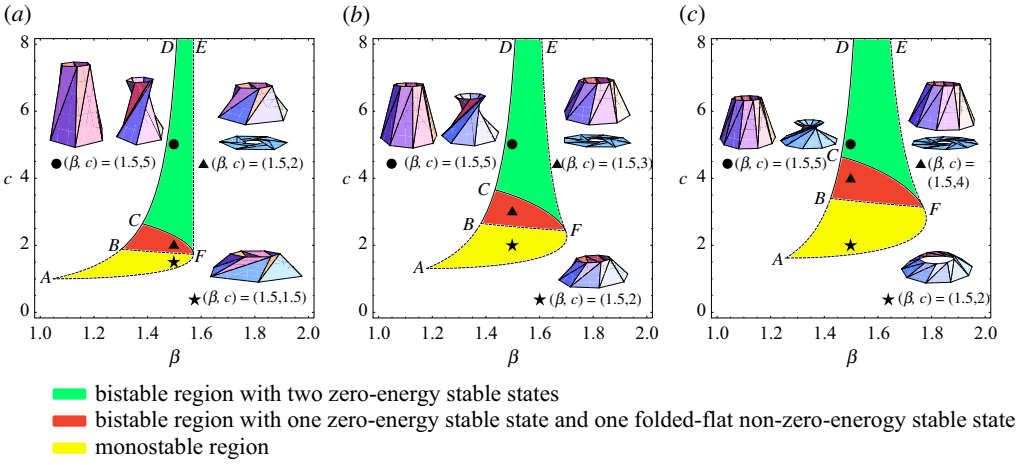

Figure 4. Phase diagrams characterizing the stable states for CKO structures with top edge length $a = 1$ and bottom edge length $b = 2$. The solid boundaries belong to the bistable area, and the dash boundaries belong to the monostable area. The insets correspond to the geometric configurations of the 'circle' symbol, the 'triangle' symbol and the 'star' symbol, respectively. The number n of unit cells is (*a*) $n = 6$, (*b*) $n = 8$ and (*c*) $n = 10$. (Online version in colour.)

the number of unit cells, the heights at the stable states decrease for both monostable and bistable CKO structures. Moreover, as the number of unit cells increases, the stable state region gradually expands.

(c) Energy landscapes

Finally, we study the energy landscapes of CKO structures. According to equation (2.2), the elastic energy U of a CKO depends on the height h and the twist angle φ. Therefore, when the two variables are independent, we can obtain an energy surface of U by varying h and φ. However, when a CKO is deployed under quasi-static tension or torsion, the two variables are coupled by $\partial U/\partial\varphi = 0$ or $\partial U/\partial h = 0$, respectively, because the force in the φ-direction (or h-direction) is zero. Consequently, the energy landscape of a CKO under quasi-static tension or torsion is a curve on the energy surface determined by $\partial U/\partial\varphi = 0$ or $\partial U/\partial h = 0$. To demonstrate this, we depict the energy landscape of a bistable CKO with two zero-energy minima in figure 5*a*. It is seen that the two energy curves are located at the valley of the energy surface, and have three intersections, which are the three stationary points (h_0, φ_0), (h_1, φ_1) and (h_2, φ_2), respectively. Figure 5*b* presents the two energy curves individually. We can observe that (h_0, φ_0) is the maximum energy point, and (h_1, φ_1) and (h_2, φ_2) are two zero-energy points, which are in consistent with our analytical solutions.

Figure 6 plots the variation of the dimensionless elastic energy with respect to the height of the CKO under quasi-static axial tension for different lengths of mountain creases c by imposing $\partial U/\partial\varphi = 0$. As can be seen, with the increase of the length of mountain creases, the height corresponding to the stable state gradually gets higher. Moreover, the energy landscapes of CKO structures with the same geometric parameters but different unit cell numbers are dramatically different. For example, when $c = 3.1$, the energy landscape of the CKO consisting of 6 unit cells has two zero-energy minima (figure 6*a*), and that consisting of 8 unit cells has one zero-energy minimum and one non-zero-energy minimum (figure 6*b*), while the CKO with 10 unit cells has only one zero-energy minimum (figure 6*c*). This suggests that the number of unit cells also has a significant influence on the energy landscapes of CKO structures.

A bistable CKO needs to overcome an energy barrier to transit from one stable state to the other. To understand the influence of geometric parameters on the energy barrier, a contour map

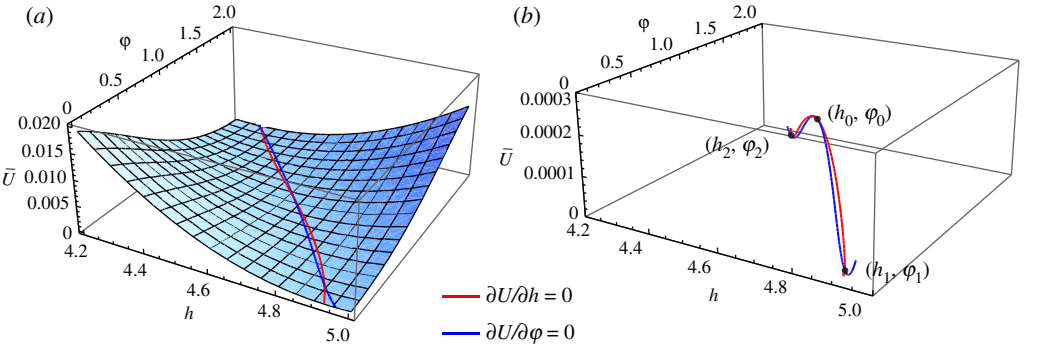

Figure 5. Variation of the dimensionless elastic energy $\bar{U}$ $(= U/EAc)$ with respect to the height h and the relative twist angle φ of a bistable CKO with two zero-energy minima. (*a*) Energy landscape. (*b*) Energy curve determined by $\partial U/\partial h = 0$ and $\partial U/\partial \varphi = 0$. Geometric parameters of the unit cells are $a = 1$, $b = 2$, $c = 5$ and $\beta = 1.5$. The number of unit cells is $n = 6$. The three stationary points are $(h_0, \varphi_0) = (4.6216, \pi/3)$, $(h_1, \varphi_1) = (4.8924, 0.1791)$ and $(h_2, \varphi_2) = (4.3185, 1.9153)$. (Online version in colour.)

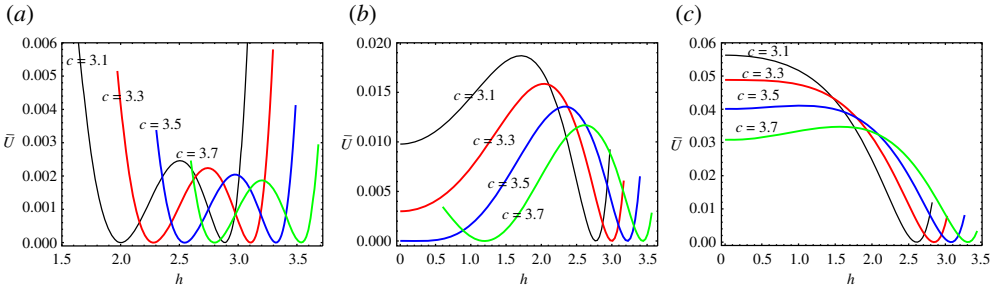

Figure 6. Variation of the dimensionless elastic energy $\bar{U}$ $(= U/EAc)$ with respect to the height h for different lengths of the mountain creases c. The remaining geometric parameters of the unit cells are $a = 1$, $b = 2$ and $\beta = 1.5$. The number n of unit cells is (*a*) $n = 6$, (*b*) $n = 8$ and (*c*) $n = 10$. (Online version in colour.)

of the dimensionless energy barrier of a bistable CKO with two zero-energy states is provided in figure 7. In this map, we fix the mountain crease c and stable-state height h_2, and then vary the values of edge length ratio a/b and stable-state height h_1. It should be noted that the energy barrier $U_{\max}$ of a bistable CKO with two zero-energy minima equals its maximum elastic energy, and when it transforms from one stable state to the other under axial force or torque (i.e. $\partial U/\partial \varphi = 0$ or $\partial U/\partial h = 0$), the maximum elastic energy always occurs at the saddle point (h_0, φ_0) (see Proofs 2 and 3 in electronic supplementary material). According to figure 7, the energy barrier of a bistable CKO decreases with the increase of the edge length ratio a/b, while increases as the stable-state height h_1 gets higher. Particularly, for a specific stable-state height and length of mountain crease, the energy barrier of a bistable CKO composed of isosceles trapezoid unit cells is the highest, which corresponds to the red boundary curve in figure 7. This contour map provides a heuristic design strategy for target energy barriers in bistable CKO structures.

3. Curvature programming

Having identified the stability characteristic, we now use CKO tessellations to approximate surfaces of revolution with various types of Gaussian curvatures. In this section, we will develop two inverse design frameworks to achieve the goal. For the first design method, we can approximate arbitrary surfaces of revolution. The approximated surfaces have rather arbitrary

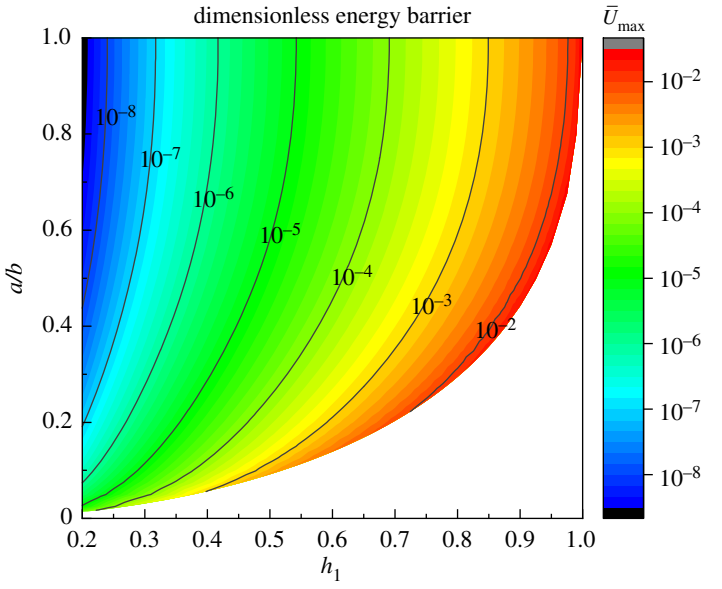

Figure 7. Contour map of the energy barrier of a bistable CKO for different values of edge length ratio a/b and stable-state height h_1. The length of the mountain crease is set to $c = 1$ and the stable-state height h_2 is fixed at $h_2 = 0$. The number of unit cells is $n = 6$. (Online version in colour.)

cross-section radii along the height direction, but are non-developable (i.e. the designed structure cannot be unfolded to a flat sheet). For the second design strategy, we can approximate surfaces of revolution whose cross-section radii are monotonic, and the obtained structures are developable. Thus the first method benefits a larger design space, while the second one has advantages in fabrication due to its developability.

Consider a CKO tessellation consisting of m layers, and each layer has n quadrilateral unit cells. As stated before, four geometric parameters are needed to characterize the unit cell. Theoretically, there are $4m$ unknown geometric parameters in total for a CKO tessellation, i.e. a_i, b_i, c_i and β_i, where the subscript i $(= 1, 2, \ldots, m)$ represents the parameters associated with the ith layer. However, since the top edge of the ith layer shares the same parameter with the bottom edge of the $(i+1)$th layer (i.e. $a_i = b_{i+1}$), there are only $3m + 1$ independent geometric parameters to be determined, which are b_i, b_{i+1}, c_i and β_i $(i = 1, 2, \ldots, m)$.

Moreover, a general surface of revolution as the target surface can be defined by

$$f(\sqrt{x^2 + y^2}, z) = 0, \quad z_1 \le z \le z_2, \tag{3.1}$$

where z_1 and z_2 are prescribed constants.

(a) Non-developable CKO tessellation

To enable the inverse design, we firstly discretize the target surface into m layers so that each segment can be approximated by a CKO unit composed of an array of quadrilateral unit cells. Here, we use bistable CKO units with two zero-energy states to achieve the design. Specifically, we exploit their first stable configurations to approximate the curved surfaces, and harness their second stable configurations to package the structures in a small space. The two stable states in the ith layer are denoted by $(h_i^{(1)}, \varphi_i^{(1)})$ and $(h_i^{(2)}, \varphi_i^{(2)})$, respectively. Then, we intend to find the

constraints for the design. Based on equations (2.13) and (2.15), and considering $a_i = b_{i+1}$ and $r_i = R_{i+1}$, the geometric parameters of the bistable CKO unit in the ith layer should satisfy

$$\sqrt{(h_i^{(1)})^2 + R_i^2 + R_{i+1}^2 - 2R_iR_{i+1}\cos\varphi_i^{(1)}} = c_i, \quad i = 1, 2, \ldots, m, \tag{3.2}$$

$$\sin\left(\varphi_i^{(1)} + \frac{\pi}{n}\right) = \frac{b_i - 2c_i\cos\beta_i}{b_{i+1}}\sin\frac{\pi}{n}, \quad i = 1, 2, \ldots, m, \tag{3.3}$$

$$\sqrt{(h_i^{(2)})^2 + R_i^2 + R_{i+1}^2 - 2R_iR_{i+1}\cos\varphi_i^{(2)}} = c_i, \quad i = 1, 2, \ldots, m \tag{3.4}$$

and

$$\sin\left(\varphi_i^{(2)} + \frac{\pi}{n}\right) = \frac{b_i - 2c_i\cos\beta_i}{b_{i+1}}\sin\frac{\pi}{n}, \quad i = 1, 2, \ldots, m. \tag{3.5}$$

Moreover, the total height of all the CKO units at the first stable state should be equal to that of the target surface of revolution, namely,

$$\sum_{i=1}^{m} h_i^{(1)} = z_2 - z_1. \tag{3.6}$$

Meanwhile, the vertices of each CKO unit at the first stable state should be located on the target surface, which gives

$$f(R_1, z_1) = 0 \quad \text{and} \quad f\left(R_{i+1}, z_1 + \sum_{j=1}^{i} h_j^{(1)}\right) = 0, \quad i = 1, 2, \ldots, m. \tag{3.7}$$

Finally, we determine the geometric parameters of each CKO unit. According to equations (3.2)–(3.7), there are $7m + 1$ unknowns including $3m + 1$ geometric parameters (i.e. b_i, b_{i+1}, c_i and β_i) and $4m$ stable-state parameters (i.e. $h_i^{(1)}$, $h_i^{(2)}$, $\varphi_i^{(1)}$ and $\varphi_i^{(2)}$). Therefore, if we prescribe the two stable-state heights $h_i^{(1)}$ and $h_i^{(2)}$ for each layer (note that $h_i^{(1)}$ should satisfy equation (3.6)), in principle, the remaining $5m + 1$ parameters (i.e. b_i, b_{i+1}, c_i, β_i, $\varphi_i^{(1)}$ and $\varphi_i^{(2)}$) of all the CKO units can be obtained layer-by-layer by solving the $5m + 1$ constraints (i.e. equations (3.2)–(3.5) and (3.7)). After determining the geometric parameters of the CKO unit in each layer, the approximated target surface of revolution can be generated by assembling the CKO units layer-by-layer. The Mathematica code for the solution is provided in electronic supplementary material data.

To illustrate the versatility of our design, we consider three typical surfaces of revolution in figure 8*a–c*, namely, a hyperboloid of revolution, an ellipsoid of revolution, and a sinusoid of revolution, as the target curved surfaces. These three surfaces show the capability of our method in approximating surfaces of revolution with negative, positive and mixed Gaussian curvatures ($K < 0$, $K > 0$, $K < 0$ and $K > 0$), respectively. For each example, we use six layers (i.e. $m = 6$) of CKO with the number of unit cells $n = 10$ for each layer to approximate the target curved surface, and presume that all the CKO units have equivalent heights at the first and second stable states ($h_i^{(1)} = (z_2 - z_1)/m$ and $h_i^{(2)} = 0$ for all i). By solving equations (3.2)–(3.5) and (3.7), we obtain the geometric parameters of the CKO unit in each layer for our inverse design (results are provided in electronic supplementary material, §S2). The numerical configurations and the paper models (fabrication details are provided in electronic supplementary material, §S7) are presented in figure 8. It can be seen that the deployed states of the CKO tessellations approximate the target surfaces of revolution well, and the folded-flat states of the CKO tessellations allow them to be packaged in a small space, which confirms the validity of our design strategy.

Remark 3.1. Note that for any given surfaces of revolution, by selecting appropriate values for parameters n, $h_i^{(1)}$ and $h_i^{(2)}$, we can always find the solutions of equations (3.2)–(3.5) and (3.7) due to the flexible design space of CKO composed of general quadrilateral unit cells. This shows that the present design strategy is applicable to approximating arbitrary surfaces of revolution. However, since this method does not consider the developability conditions between adjacent layers, the designed CKO tessellations cannot be guaranteed to be developable. In other words, the 3D structures cannot be unfolded into flat sheets. Although this issue will increase the

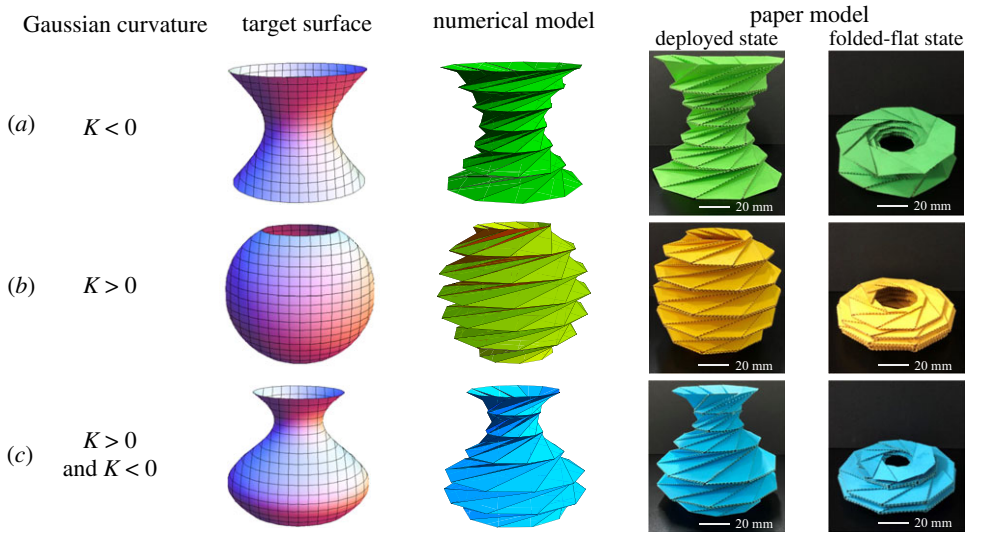

Figure 8. Approximations of target surfaces of revolution by using non-developable CKO tessellations. (*a*) Hyperboloid of revolution with negative Gaussian curvature ($K < 0$). The function of the target surface is $(x^2 + y^2)/9 - (3z^2)/25 = 1$ with $-5 \le z \le 5$. (*b*) Ellipsoid of revolution with positive Gaussian curvature ($K > 0$). The function of the target surface is $(x^2 + y^2)/36 + (3z^2)/100 = 1$ with $-5 \le z \le 5$. (*c*) Sinusoid of revolution with mixed curvature ($K < 0$ and $K > 0$). The function of the target surface is $\sqrt{x^2 + y^2} = 2\sin(-0.6z) + 4$ with $-5 \le z \le 5$. (Online version in colour.)

difficulty in manufacturing the origami structures, it can be overcome by using other methods, for example, 3D printing.

(b) Developable CKO tessellation

Next, we show how to approximate target surfaces of revolution using CKO tessellations which are developable. The crease pattern of a developable CKO tessellation is shown in figure 9*a*, which comprises $m \times n$ quadrilateral unit cells and each unit cell can be characterized by b_i, b_{i+1}, c_i and β_i ($i = 1, 2, \ldots, m$). The developability condition can be determined in terms of the geometric parameters of the CKO.

(i) Developability condition

The condition for a CKO tessellation that can be folded from a flat sheet (i.e. developable) is that at each interior vertex, the sum of the angles between the adjacent edges equals 2π (figure 9*b*), which reads

$$\alpha_i + \beta_i + \gamma_{i-1} + \delta_{i-1} = 2\pi, \quad i = 2, 3, \ldots, m. \tag{3.8}$$

Considering $\gamma_{i-1} + \delta_{i-1} = 2\pi - \alpha_{i-1} - \beta_{i-1}$, the developability condition can be rewritten as

$$\alpha_i + \beta_i = \alpha_{i-1} + \beta_{i-1}, \quad i = 2, 3, \ldots, m, \tag{3.9}$$

in which

$$\alpha_i = \arccos\left(\frac{b_i^2 + d_i^2 - c_i^2}{2b_i d_i}\right) + \arccos\left(\frac{c_i^2 + d_i^2 - b_{i+1}^2}{2c_i d_i}\right), \quad i = 1, 2, \ldots, m. \tag{3.10}$$

It can be seen from equations (3.9) and (3.10) that the geometric parameters (b_i, b_{i+1}, c_i, β_i) are all incorporated in the developability condition. Combining it with the constraints in §3a, the inverse problem for developable CKO tessellations that approximate target surfaces of revolution can be solved.

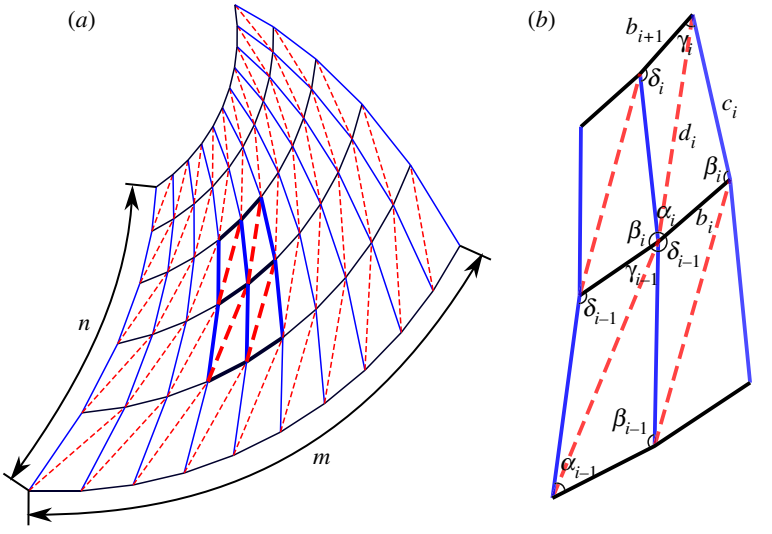

Figure 9. Crease pattern of a developable CKO tessellation. (*a*) Schematic of the crease pattern consisting of $m \times n$ quadrilateral unit cells. (*b*) Schematic of four adjacent unit cells sharing a vertex with the labels of geometric parameters. (Online version in colour.)

(ii) Inverse design framework

There are $6m+1$ constraints (i.e. equations (3.2)–(3.7) and (3.9)), and $7m+1$ unknown variables (i.e. b_i, b_{i+1}, c_i, β_i, $h_i^{(1)}$, $h_i^{(2)}$, $\varphi_i^{(1)}$ and $\varphi_i^{(2)}$). In the following, we prescribe the stable-state height $h_i^{(2)}$ so that the number of variables equals that of constraints, leading to a closed solvable equation system. Specifically, similar to the previous case, we assume that the CKO tessellation has a folded-flat zero-energy stable state, i.e. $h_i^{(2)}=0$. We then employ an optimization algorithm to solve the inverse problem for the CKO tessellation.

The unknown parameters (b_i, b_{i+1}, c_i, β_i, $h_i^{(1)}$, $\varphi_i^{(1)}$, $\varphi_i^{(2)}$) are selected as the optimization variables, and their initial values for the optimization inherit from the analytical method in §3a. Equations (3.2)–(3.6) and (3.9) are set as the constraints, and the square of equation (3.7) is chosen as the objective function. In summary, the optimization problem can be described as

$$\left.\begin{aligned}
&\text{Find}: (b_i, b_{i+1}, c_i, \beta_i, h_i^{(1)}, \varphi_i^{(1)}, \varphi_i^{(2)}), \quad i=1,2,\ldots,m.\\
&\text{Minimize}: [f(R_1,z_1)]^2 \quad \text{and} \quad \left[f(R_{i+1}, z_1+\sum_{k=1}^{i} h_k^{(1)})\right]^2, \quad i=1,2,\ldots,m.\\
&\text{s.t.}: \begin{cases}
c_i^2 - R_i^2 - R_{i+1}^2 + 2R_iR_{i+1}\cos\varphi_i^{(1)} - [h_i^{(1)}]^2 = 0, & i=1,2,\ldots,m,\\
\sin\left(\varphi_i^{(1)}+\frac{\pi}{n}\right) - \frac{(b_i - 2c_i\cos\beta_i)\sin(\pi/n)}{b_{i+1}} = 0, & i=1,2,\ldots,m,\\
c_i^2 - R_i^2 - R_{i+1}^2 + 2R_iR_{i+1}\cos\varphi_i^{(2)} - [h_i^{(2)}]^2 = 0, & i=1,2,\ldots,m,\\
\sin\left(\varphi_i^{(2)}+\frac{\pi}{n}\right) - \frac{(b_i - 2c_i\cos\beta_i)\sin(\pi/n)}{b_{i+1}} = 0, & i=1,2,\ldots,m.\\
\sum_{i=1}^{m} h_i^{(1)} - (z_2 - z_1) = 0,\\
\alpha_i + \beta_i - \alpha_{i-1} - \beta_{i-1} = 0, & i=2,3,\ldots,m.
\end{cases}
\end{aligned}\right\} \tag{3.11}$$

By using the multiobjective optimization function *fgoalattain* in Matlab, the geometric parameters of a developable CKO tessellation that approximates a target surface of revolution can be determined. The Matlab code for the optimization is given in electronic supplementary material data. To demonstrate this design method, we use a CKO tessellation with $m=6$ and $n=10$ to

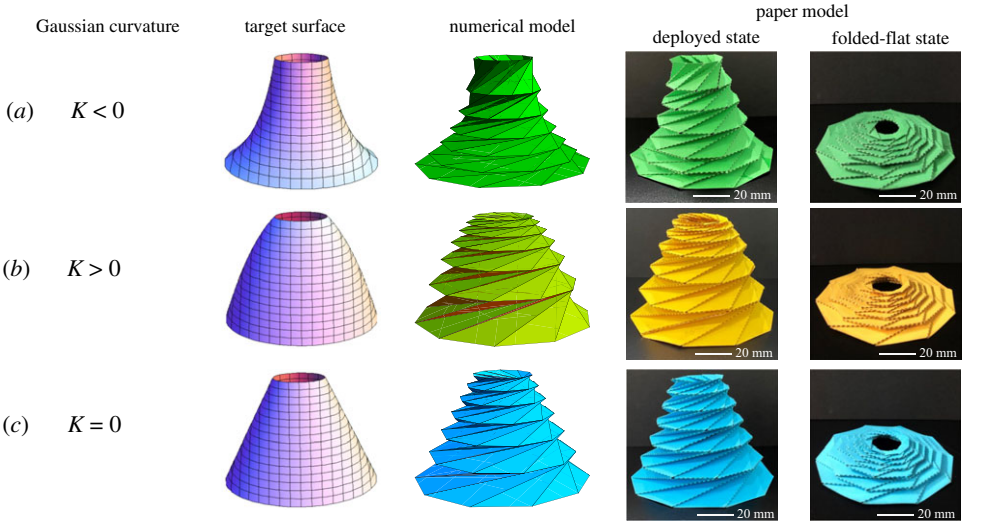

Figure 10. Approximations of target surfaces of revolution by using developable CKO tessellations. (*a*) Hyperboloid of revolution with negative Gaussian curvature ($K < 0$). The function of the target surface is $(z + 6)\sqrt{x^2 + y^2} = 54$ with $0 \leq z \leq 12$. (*b*) Paraboloid of revolution with positive Gaussian curvature ($K > 0$). The function of the target surface is $x^2 + y^2 + 6z = 81$ with $0 \leq z \leq 12$. (*c*) Cone of revolution with zero Gaussian curvature ($K = 0$). The function of the target surface is $2\sqrt{x^2 + y^2} + z = 18$ with $0 \leq z \leq 12$. (Online version in colour.)

approximate various surfaces of revolution shown in figure 10*a–c*. By employing the proposed optimization algorithm, we obtain the optimized geometric parameters of the CKO tessellation, which are provided in electronic supplementary material, §S3. With the help of laser cutter, we fabricate the corresponding paper models (fabrication details refer to electronic supplementary material, §S7). From figure 10, one can see that the deployed states of the CKO tessellations folded from a flat sheet closely approach the target surfaces of revolution with different types of Gaussian curvatures. Also, our paper models show that the designed CKO tessellations are flat-foldable.

Remark 3.2. It is worth noting that the developable CKO tessellations can only approximate surfaces of revolution whose cross-section radii along the height direction are monotonic. If the radii are not monotonic, the slope of the generator of the surface will change the sign in the direction along its height (see the three target surfaces in figure 8) and therefore a segment containing a point with infinite slope emerges. At this segment, a TKO cell is required to connect with other layers. However, the developability condition cannot be satisfied in this case, since $\alpha_i + \beta_i = \pi$ for a TKO pattern while $\alpha_i + \beta_i \neq \pi$ for a CKO pattern. Thus, the assembly of a TKO and a CKO is non-developable.

(iii) Discussion

Approximating 3D curved surfaces has been achieved in various types of origami, such as the Miura origami [24] and the waterbomb origami [28]. Compared to the degree-4 vertex Miura cells and the degree-6 vertex waterbomb cells, our CKO cells have only one diagonal crease, greatly reducing the difficulty in manufacturing the physical models. In addition, the relatively simple crease pattern also simplifies the design method as well as improves the computational efficiency. For example, our design equations for the non-developable CKO tessellation can be analytically solved, and our optimization algorithm for the developable CKO tessellation can converge to the optimal solutions in just a few seconds. Consequently, the origami tool and methodology proposed in the present work provide a simple and efficient strategy for the inverse design of 3D surfaces of revolution.

4. Energy programming

Energy barrier and stable-state height are two key parameters in characterizing the mechanical performance of bistable or multistable structures [50,51]. In this section, we will demonstrate how to design a multistable CKO tessellation with prescribed energy barriers and stable-state heights. For this goal, we formulate a multiobjective optimization problem. Specifically, we consider a CKO tessellation consisting of m layers, in which the CKO unit in the ith ($i = 1, 2, \ldots, m$) layer has two zero-energy stable states at the heights $h_i^{(1)}$ and $h_i^{(2)}$ and attains an energy barrier $U_i^{\max}$. The parameters to be determined are the geometric parameters (b_i, b_{i+1}, c_i, β_i) of the CKO cells, the height $h_i^{(0)}$ corresponding to the maximum elastic energy (i.e. the energy barrier), and the relative twist angles $\varphi_i^{(1)}$ and $\varphi_i^{(2)}$ associated with the stable-state height $h_i^{(1)}$ and $h_i^{(2)}$. To establish a general design framework, all the parameters are non-dimensionalized by

$$\bar{b}_i = \frac{b_i}{c_1},\ \bar{b}_{i+1} = \frac{b_{i+1}}{c_1},\ \bar{c}_i = \frac{c_i}{c_1},\ \bar{h}_i^{(0)} = \frac{h_i^{(0)}}{c_1},\ \bar{U}_i^{\max} = \frac{U_i^{\max}}{EAc_1},\quad i = 1, 2, \ldots, m. \tag{4.1}$$

For real demonstrations, one can rescale the target quantities such as the energy barrier with corresponding parameters. Note that we specify $c_1 = 1$ in all the examples.

When the energy barrier $\bar{U}_i^{\max}$ and two stable-state heights $\bar{h}_i^{(1)}$ and $\bar{h}_i^{(2)}$ of the CKO unit in each layer are prescribed, the unknown parameters should satisfy the following relations:

- The geometric parameters ($\bar{b}_i$, $\bar{b}_{i+1}$, $\bar{c}_i$, β_i) and the relative twist angle $\varphi_i^{(1)}$ and $\varphi_i^{(2)}$ should satisfy the stability conditions equations (3.2)–(3.5).
- The height $\bar{h}_i^{(0)}$ and the relative twist angle $\varphi_i^{(0)}$ corresponding to the maximum elastic energy should satisfy equation (2.9), in which $\varphi_i^{(0)} = \pi/2 - \pi/n$.
- The maximum elastic energy $\bar{U}_i(\bar{h}_i^{(0)}, \varphi_i^{(0)})$ should be equal to the target energy barrier $\bar{U}_i^{\max}$.

By selecting equations (3.2)–(3.5) and (2.9) as the constraints, and the difference between the maximum elastic energy and the target energy barrier as the objective function, the optimization problem can be formulated as

$$\begin{aligned}
&\text{Find}: (\bar{b}_i, \bar{b}_{i+1}, \bar{c}_i, \beta_i, \bar{h}_i^{(0)}, \varphi_i^{(1)}, \varphi_i^{(2)}),\quad i = 1, 2, \ldots, m.\\
&\text{Minimize}: k[\bar{U}_i(\bar{h}_i^{(0)}, \varphi_i^{(0)}) - \bar{U}_i^{\max}]^2,\quad i = 1, 2, \ldots, m.\\
&\text{s.t.}: \begin{cases}
\bar{c}_i^2 - \bar{R}_i^2 - \bar{R}_{i+1}^2 + 2\bar{R}_i\bar{R}_{i+1}\cos\varphi_i^{(1)} - [\bar{h}_i^{(1)}]^2 = 0, & i = 1, 2, \ldots, m,\\
\sin\left(\varphi_i^{(1)} + \frac{\pi}{n}\right) - \frac{(\bar{b}_i - 2\bar{c}_i\cos\beta_i)\sin(\pi/n)}{\bar{b}_{i+1}} = 0, & i = 1, 2, \ldots, m,\\
\bar{c}_i^2 - \bar{R}_i^2 - \bar{R}_{i+1}^2 + 2\bar{R}_i\bar{R}_{i+1}\cos\varphi_i^{(2)} - [\bar{h}_i^{(2)}]^2 = 0, & i = 1, 2, \ldots, m,\\
\sin\left(\varphi_i^{(2)} + \frac{\pi}{n}\right) - (\bar{b}_i - 2\bar{c}_i\cos\beta_i)\sin\left(\frac{\pi}{n}\right)/\bar{b}_{i+1} = 0, & i = 1, 2, \ldots, m.\\
\frac{1}{\bar{c}_i} - \frac{1}{\bar{c}_i(\bar{h}_i^{(0)}, \varphi_i^0)} + \frac{1}{\bar{d}_i} - \frac{1}{\bar{d}_i(\bar{h}_i^{(0)}, \varphi_i^0)} = 0, & i = 1, 2, \ldots, m,\\
\bar{c}_1 = 1
\end{cases}
\end{aligned} \tag{4.2}$$

Here, we premultiply a factor k in the objective function to amplify the magnitude of the error and hence improve the accuracy of the optimization. The optimization problem described in equation (4.2) can be solved by the function *fgoalattain* in Matlab, and the related code is provided in electronic supplementary material data. The accuracy of the optimized results significantly depends on the initial values of the variables, and the details of how to find ideal initial values are presented in electronic supplementary material.

Remark 4.1. From equation (4.2), we find that there are m objective functions and $5m + 1$ independent constraints, then the total number $(6m + 1)$ is exactly equal to the number of

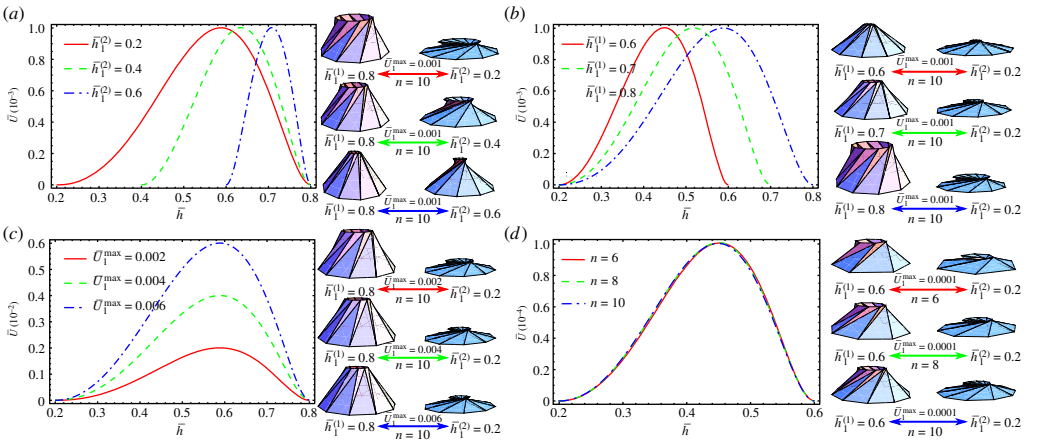

Figure 11. Optimized energy landscapes and stable-state configurations of bistable CKO structures. The target parameters are set as (*a*) $\bar{h}_1^{(1)} = 0.8, \bar{h}_1^{(2)}$=[0.2, 0.4, 0.6] and $\bar{U}_1^{\max} = 0.001$; (*b*) $\bar{h}_1^{(1)} = [0.6, 0.7, 0.8], \bar{h}_1^{(2)} = 0.2$ and $\bar{U}_1^{\max} = 0.001$; (*c*) $\bar{h}_1^{(1)} = 0.8$, $\bar{h}_1^{(2)} = 0.2$ and $\bar{U}_1^{\max} = [0.002, 0.004, 0.006]$; (*d*) $\bar{h}_1^{(1)} = 0.6, \bar{h}_1^{(2)} = 0.2$ and $\bar{U}_1^{\max} = 0.0001$. (Online version in colour.)

optimization variables. Therefore, (4.2) is closed, suggesting that the energy landscape of a CKO tessellation can be programmed by our optimization framework. However, for a TKO tessellation, we have $b_i = b_{i+1}$, then the number of optimization variables are reduced to $5m + 1$, which is less than the sum of constraints and objective functions. Consequently, the optimization problem in this case is over-constrained, which indicates that the TKO tessellation is not capable of programming all the stable-state heights and energy barriers simultaneously.

To demonstrate the design strategy, we firstly consider several examples in figure 11 for the inverse design of bistable CKO with various target energy barriers and stable-state heights. In each example, there are three target parameters, i.e. $\bar{h}_1^{(1)}$, $\bar{h}_1^{(2)}$ and $\bar{U}_1^{\max}$. For the examples in figure 11*a–c*, we set two of them to be the same but change the remaining one, and then use 10 unit cells to find the optimal solutions. The target parameters of these examples are provided in the caption of figure 11. The optimized results for the geometric parameters are given in electronic supplementary material, table S6. By using these geometric parameters, we plot the corresponding energy landscapes as well as the stable-state configurations of the designed CKO structures. The energy landscapes of these structures all exhibit typical bistability characteristics. More importantly, the stable-state heights and energy barriers are in great agreement with the target parameters. In figure 11*d*, the three target parameters of each example are all set to be the same, while we use 6, 8 and 10 unit cells to explore the optimal solutions, respectively. The optimized results are also presented in electronic supplementary material, table S6. It is seen from figure 11*d* that with the same target parameters but different numbers of unit cells, the optimized energy curves nearly overlap, showing that the number of unit cells is less important in this optimization. These examples indicate that the proposed optimization algorithm is effective and accurate for the inverse design of bistable CKO with the prescribed energy barrier and stable-state heights.

Next, we present two examples, a bilayer CKO tessellation and a trilayer CKO tessellation, in figure 12 for the inverse design of multistable CKO tessellations with predefined stable-state parameters. The target parameters of the two examples are given in the caption of figure 12. By selecting appropriate initial values and factor k, we obtain the optimized geometric parameters of the two CKO tessellations and the results are enclosed in §S5 of electronic supplementary material. With these parameters, figure 12*a*,*b* depicts the optimized energy landscapes of the bilayer and trilayer CKO tessellations, respectively. As can be seen, the bilayer and trilayer CKO tessellations undergo three and four stable states, respectively, upon folding. In particular, both

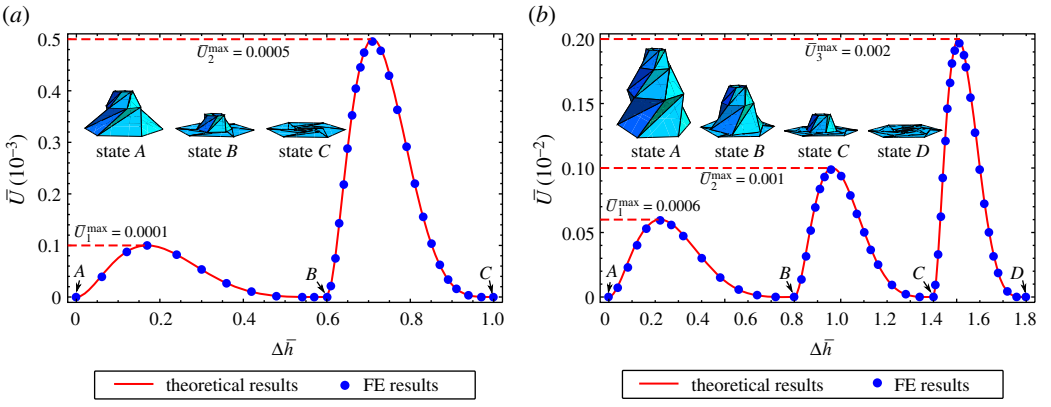

Figure 12. Optimized energy landscapes and stable-state configurations of multistable CKO tessellations. (*a*) A bilayer CKO tessellation with target $[\bar{h}_1^{(1)}, \bar{h}_1^{(2)}, \bar{U}_1^{\max}] = [0.6, 0, 0.0001]$ and $[\bar{h}_2^{(1)}, \bar{h}_2^{(2)}, \bar{U}_2^{\max}] = [0.4, 0, 0.0005]$. (*b*) A trilayer CKO tessellation with target $[\bar{h}_1^{(1)}, \bar{h}_1^{(2)}, \bar{U}_1^{\max}] = [0.8, 0, 0.0006]$, $[\bar{h}_2^{(1)}, \bar{h}_2^{(2)}, \bar{U}_2^{\max}] = [0.6, 0, 0.001]$ and $[\bar{h}_3^{(1)}, \bar{h}_3^{(2)}, \bar{U}_3^{\max}] = [0.4, 0, 0.002]$. The bottom layer corresponds to the first layer represented by the subscript 1. (Online version in colour,)

of them collapse sequentially according to the energy barrier of each layer from low to high. To verify the theoretical results, we perform FE simulations for the quasi-static compression process of the two designed CKO tessellations, and obtain the elastic energy associated with different displacements. The details of the FE simulations are provided in §S6 of electronic supplementary material, and the results are presented in figure 12. The figures show excellent agreements between the results of our theoretical modelling and the FE simulations. More importantly, both results perfectly approach the target parameters, which demonstrates that our strategy is robust and capable of achieving a series of target stable-state parameters for multistable CKO tessellations. We also observe from the simulations that when the first layer collapses, the other layers also deform. However, the deformations of the other layers are much smaller than those of the collapsed layer due to their higher effective stiffness. To illustrate this, we provide the energy curve of each layer and the force–displacement curves of the two CKO tessellations during the entire folding process obtained by FE simulations in electronic supplementary material, §S6. The results confirm that the remaining layers experience negligible deformations when the first layer collapses. Furthermore, since our design method for programming energy is based on the elastic truss model, we provide an effective strategy for designing origami-based multistable truss structures with programmable mechanical properties.

5. Concluding remarks

In this work, we have developed a generalized design framework for conical Kresling origami composed of general quadrilateral unit cells. Through theoretical modelling and analysis, we obtain the analytical solutions and the design spaces of its stable states, and then identify the effect of geometric parameters on its energy landscape. We find that by employing free-form quadrilateral unit cells, the design space of traditional Kresling origami can be enlarged without loss of its remarkable bistability characteristic. Importantly, benefiting from the additional degrees of freedom offered by the general quadrilateral unit cells, the conical Kresling origami enables many useful designs which cannot be achieved by the traditional Kresling pattern, such as programming curvature of curved surfaces and programming energy landscapes of multistable structures. Therefore, the present work provides a new perspective for the design of deployable structures, including shape-morphing devices, reconfigurable space antennas, fluidic soft actuators and multi-modal robots. Also, the conical Kresling origami can serve as a powerful

tool to design multistable metamaterials with desired energy absorption ability or deformation sequence.

Data accessibility. The electronic supplementary material supporting this article are available online.

Authors' contributions. L.L., F.F. and H.D. convinced the idea and designed the research. L.L., X.D. and F.F. built the models and analysed the results. L.L. conducted the numerical simulations. L.L., X.D. and P.L. fabricated the paper models. L.L., F.F. and H.D. wrote the manuscript. All authors discussed the results, commented on the manuscript and approved the manuscript for publication.

Competing interests. We declare we have no competing interests.

Funding. This work was supported by the National Natural Science Foundation of China (grant nos. 91848201, 11988102 and 11872004), the National Key R&D Program of China (grant no. 2020YFE0204200) and China Postdoctoral Science Foundation (grant no. 2020TQ0006).

Acknowledgements. We thank the anonymous reviewers whose insightful comments and suggestions have significantly improved the quality of this work.

References

1. Schenk M, Guest SD. 2013 Geometry of Miura-folded metamaterials. *Proc. Natl Acad. Sci. USA* **110**, 3276–3281. (doi:10.1073/pnas.1217998110)
2. Wei ZY, Guo ZV, Dudte L, Liang HY, Mahadevan L. 2013 Geometric mechanics of periodic pleated origami. *Phys. Rev. Lett.* **110**, 215501. (doi:10.1103/PhysRevLett.110.215501)
3. Feng F, Dang X, James RD, Plucinsky P. 2020 The designs and deformations of rigidly and flat-foldable quadrilateral mesh origami. *J. Mech. Phys. Solids* **142**, 104018. (doi:10.1016/j.jmps.2020.104018)
4. Tachi T. 2009 Generalization of rigid-foldable quadrilateral-mesh origami. *J. Int. Assoc. Shell Spat. Struct.* **50**, 173–179.
5. Feng F, Plucinsky P, James RD. 2020 Helical Miura origami. *Phys. Rev. E* **101**, 033002. (doi:10.1103/PhysRevE.101.033002)
6. Waitukaitis S, Menaut R, Chen BG, van Hecke M. 2015 Origami multistability: from single vertices to metasheets. *Phys. Rev. Lett.* **114**, 055503. (doi:10.1103/PhysRevLett.114.055503)
7. Zirbel SA, Lang RJ, Thomson MW, Sigel DA, Walkemeyer PE, Trease BP, Magleby SP, Howell LL. 2013 Accommodating thickness in origami-based deployable arrays. *ASME J. Mech. Des.* **135**, 111005. (doi:10.1115/1.4025372)
8. Kuribayashi K, Tsuchiya K, You Z, Tomus D, Umemoto M, Ito T, Sasaki M. 2006 Self-deployable origami stent grafts as a biomedical application of Ni-rich TiNi shape memory alloy foil. *Mater. Sci. Eng. A* **419**, 131–137. (doi:10.1016/j.msea.2005.12.016)
9. Boatti E, Vasios N, Bertoldi K. 2017 Origami metamaterials for tunable thermal expansion. *Adv. Mater.* **29**, 1700360. (doi:10.1002/adma.v29.26)
10. Fang H, Chu SCA, Xia Y, Wang KW. 2018 Programmable self-locking origami mechanical metamaterials. *Adv. Mater.* **30**, 1706311. (doi:10.1002/adma.v30.15)
11. Liu K, Tachi T, Paulino GH. 2019 Invariant and smooth limit of discrete geometry folded from bistable origami leading to multistable metasurfaces. *Nat. Commun.* **10**, 4238. (doi:10.1038/s41467-019-11935-x)
12. Pratapa PP, Suryanarayana P, Paulino GH. 2018 Bloch wave framework for structures with nonlocal interactions: application to the design of origami acoustic metamaterials. *J. Mech. Phys. Solids* **118**, 115–132. (doi:10.1016/j.jmps.2018.05.012)
13. Silverberg JL, Evans AA, McLeod L, Hayward RC, Hull T, Santangelo CD, Cohen I. 2014 Using origami design principles to fold reprogrammable mechanical metamaterials. *Science* **345**, 647–650. (doi:10.1126/science.1252876)
14. Filipov ET, Liu K, Tachi T, Schenk M, Paulino GH. 2017 Bar and hinge models for scalable analysis of origami. *Int. J. Solids Struct.* **124**, 26–45. (doi:10.1016/j.ijsolstr.2017.05.028)
15. Chen Y, Peng R, You Z. 2015 Origami of thick panels. *Science* **349**, 396–400. (doi:10.1126/science.aab2870)
16. Filipov ET, Tachi T, Paulino GH. 2015 Origami tubes assembled into stiff, yet reconfigurable structures and metamaterials. *Proc. Natl Acad. Sci. USA* **112**, 12 321–12 326. (doi:10.1073/pnas.1509465112)
17. Li S, Fang H, Sadeghi S, Bhovad P, Wang KW. 2019 Architected origami materials: how folding creates sophisticated mechanical properties. *Adv. Mater.* **31**, 1805282. (doi:10.1002/adma.v31.5)

18. Melancon D, Gorissen B, García-Mora CJ, Hoberman C, Bertoldi K. 2021 Multistable inflatable origami structures at the metre scale. *Nature* **592**, 545–550. (doi:10.1038/s41586-021-03407-4)
19. Kim W, Byun J, Kim JK, Choi WY, Jakobsen K, Jakobsen J, Lee DY, Cho KJ. 2019 Bioinspired dual-morphing stretchable origami. *Sci Robot.* **4**, eaay3493. (doi:10.1126/scirobotics.aay3493)
20. Rus D, Tolley MT. 2018 Design, fabrication and control of origami robots. *Nat. Rev. Mater.* **3**, 101–112. (doi:10.1038/s41578-018-0009-8)
21. Zhai Z, Wang Y, Lin K, Wu L, Jiang H. 2020 In situ stiffness manipulation using elegant curved origami. *Sci. Adv.* **6**, eabe2000. (doi:10.1126/sciadv.abe2000)
22. Callens SJP, Zadpoor AA. 2018 From flat sheets to curved geometries: origami and kirigami approaches. *Mater. Today* **21**, 241–264. (doi:10.1016/j.mattod.2017.10.004)
23. Dang X, Feng F, Plucinsky P, James RD, Duan H, Wang J. 2022 Inverse design of deployable origami structures that approximate a general surface. *Int. J. Solids Struct.* **234–235**, 111224. (doi:10.1016/j.ijsolstr.2021.111224)
24. Dudte LH, Vouga E, Tachi T, Mahadevan L. 2016 Programming curvature using origami tessellations. *Nat. Mat.* **15**, 583–588. (doi:10.1038/nmat4540)
25. Hu Y, Liang H, Duan H. 2019 Design of cylindrical and axisymmetric origami structures based on generalized Miura-ori cell. *ASME J. Mech. Rob.* **11**, 051004. (doi:10.1115/1.4043800)
26. Song K, Zhou X, Zang S, Wang H, You Z. 2017 Design of rigid-foldable doubly curved origami tessellations based on trapezoidal crease patterns. *Proc. R. Soc. A* **473**, 20170016. (doi:10.1098/rspa.2017.0016)
27. Tachi T. 2013 Designing freeform origami tessellations by generalizing Resch's patterns. *ASME J. Mech. Des.* **135**, 111006. (doi:10.1115/1.4025389)
28. Zhao Y, Endo Y, Kanamori Y, Mitani J. 2018 Approximating 3D surfaces using generalized waterbomb tessellations. *J. Comput. Des. Eng.* **5**, 442–448.
29. Miura K. 1985 Method of packaging and deployment of large membranes in space. *Inst. Space Astronaut. Sci. Rep.* **618**, 1–9.
30. Kresling B. 2008 Natural twist buckling in shells: from the Hawkmoth's bellows to the deployable Kresling-pattern and cylindrical Miura-ori. In *Proc. of the 6th Int. Conf. on Computation of Shell and Spatial Structures, Ithaca, NY, 28–31 May* (eds JF Abel, JR Cooke), pp. 1–4.
31. Silverberg JL, Na JH, Evans AA, Liu B, Hull TC, Santangelo CD, Lang RJ, Hayward RC, Cohen I. 2015 Origami structures with a critical transition to bistability arising from hidden degrees of freedom. *Nat. Mater.* **14**, 389–393. (doi:10.1038/nmat4232)
32. Chen Y, Feng H, Ma J, Peng R, You Z. 2016 Symmetric waterbomb origami. *Proc. R. Soc. A* **472**, 20150846. (doi:10.1098/rspa.2015.0846)
33. Cai J, Deng X, Zhou Y, Feng J, Tu Y. 2015 Bistable behavior of the cylindrical origami structure with Kresling pattern. *ASME J. Mech. Des.* **137**, 061406. (doi:10.1115/1.4030158)
34. Kidambi N, Wang KW. 2020 Dynamics of Kresling origami deployment. *Phys. Rev. E* **101**, 063003. (doi:10.1103/PhysRevE.101.063003)
35. Masana R, Daqaq MF. 2019 Equilibria and bifurcations of a foldable paper-based spring inspired by Kresling-pattern origami. *Phys. Rev. E* **100**, 063001. (doi:10.1103/PhysRevE.100.063001)
36. Li Z, Kidambi N, Wang L, Wang KW. 2020 Uncovering rotational multifunctionalities of coupled Kresling modular structures. *Extreme Mech. Lett.* **39**, 100795. (doi:10.1016/j.eml.2020.100795)
37. Tao R, Ji LT, Li Y, Wan ZS, Hu WX, Wu WW, Liao BB, Ma LH, Fang DN. 2020 4D printed origami metamaterials with tunable compression twist behavior and stress strain curves. *Compos. Part B Eng.* **201**, 108344. (doi:10.1016/j.compositesb.2020.108344)
38. Zhai Z, Wang Y, Jiang H. 2018 Origami-inspired, on-demand deployable and collapsible mechanical metamaterials with tunable stiffness. *Proc. Natl Acad. Sci. USA* **115**, 2032–2037. (doi:10.1073/pnas.1720171115)
39. Yasuda H, Miyazawa Y, Charalampidis EG, Chong C, Kevrekidis PG, Yang Y. 2019 Origami-based impact mitigation via rarefaction solitary wave creation. *Sci. Adv.* **5**, eaau2835. (doi:10.1126/sciadv.aau2835)
40. Bhovad P, Kaufmann J, Li S. 2019 Peristaltic locomotion without digital controllers: exploiting multi-stability in origami to coordinate robotic motion. *Extreme Mech. Lett.* **32**, 100552. (doi:10.1016/j.eml.2019.100552)
41. Kaufmann J, Bhovad P, Li S. In press. Harnessing the multi-stability of Kresling origami for reconfigurable articulation in soft robotic arms. *Soft Robot*. (doi:10.1089/soro.2020.0075)

42. Pagano A, Yan T, Chien B, Wissa A, Tawfick S. 2017 A crawling robot driven by multi-stable origami. *Smart Mater. Struct.* **26**, 094007. (doi:10.1088/1361-665X/aa721e)
43. Fang H, Chang TS, Wang KW. 2020 Magneto-origami structures: engineering multi-stability and dynamics via magneticelastic coupling. *Smart Mater. Struct.* **29**, 015026. (doi:10.1088/1361-665X/ab524e)
44. Novelino LS, Ze Q, Wu S, Paulino GH, Zhao R. 2020 Untethered control of functional origami microrobots with distributed actuation. *Proc. Natl Acad. Sci. USA* **117**, 24 096–24 101. (doi:10.1073/pnas.2013292117)
45. Yasuda H, Tachi T, Lee M, Yang J. 2017 Origami-based tunable truss structures for non-volatile mechanical memory operation. *Nat. Commun.* **8**, 1–7. (doi:10.1038/s41467-017-00670-w)
46. Shah SIH, Lim S. 2021 Review on recent origami inspired antennas from microwave to terahertz regime. *Mater. Des.* **198**, 109345. (doi:10.1016/j.matdes.2020.109345)
47. Li Y, You Z. 2019 Origami concave tubes for energy absorption. *Int. J. Solids Struct.* **169**, 21–40. (doi:10.1016/j.ijsolstr.2019.03.026)
48. Xiang XM, Lu G, You Z. 2020 Energy absorption of origami inspired structures and materials. *Thin-Walled Struct.* **157**, 107130. (doi:10.1016/j.tws.2020.107130)
49. Liu K, Paulino GH. 2017 Nonlinear mechanics of non-rigid origami: an efficient computational approach. *Proc. R. Soc. A* **473**, 20170348. (doi:10.1098/rspa.2017.0348)
50. Che K, Yuan C, Wu J, Qi HJ, Meaud J. 2017 Three-dimensional-printed multistable mechanical metamaterials with a deterministic deformation sequence. *ASME J. Appl. Mech.* **84**, 011004. (doi:10.1115/1.4034706)
51. Li Y, Pellegrino S. 2020 A theory for the design of multi-stable morphing structures. *J. Mech. Phys. Solids* **136**, 103772. (doi:10.1016/j.jmps.2019.103772)